Available online at www.sciencedirect.com
SCIENCE DIRECT
Journal of Catalysis 230 (2005) 173–185
JOURNAL OF CATALYSIS
www.elsevier.com/locate/jcat

Stability, structure, and oxidation state of Mo/H-ZSM-5 catalysts during reactions of CH_4 and CH_4–CO_2 mixtures

Howard S. Lacheen, Enrique Iglesia *

Department of Chemical Engineering, University of California at Berkeley, Berkeley, CA 94720, USA

Received 1 October 2004; revised 25 November 2004; accepted 29 November 2004

Abstract

$Mo_2O_5^{2+}$-ZSM-5 ($Mo/Al_f = 0.4$, $Si/Al_f = 20$) samples prepared by sublimation of MoO_3 were carburized in CH_4 to form MoC_x clusters active in CH_4 pyrolysis and then exposed to different CO_2/CH_4 mixtures. CO_2/CH_4 reactant ratios between 0 and 0.1 increased catalyst stability but decreased pyrolysis rates, and ratios above 0.1 led to a sudden loss of activity that was reversed after removal of CO_2. Below CO_2/CH_4 ratios of 0.1, the catalyst bed can be described as a CO_2-reforming and pyrolysis reactor in series. In the first segment of the bed, where CO_2 is present, pyrolysis is completely suppressed by reverse Boudouard reactions; pyrolysis reactions begin after CO_2 is completely consumed. CO_2 cannot directly influence rates or deactivation for pyrolysis reactions. Rather, the greater stability observed with CO_2-containing reactants arises solely from the presence of H_2, formed in the CO_2-reforming section, in the pyrolysis regions within the catalyst bed. The evolution of catalyst structure and composition in CO_2/CH_4 reactants was also probed by mass spectrometric analysis of effluent streams and by in situ X-ray absorption spectroscopy to determine the underlying processes responsible for reversible deactivation at CO_2/CH_4 ratios greater than 0.1. MoC_x-ZSM-5 samples exposed to CO_2/CH_4 streams with 0.022 and 0.055 ratios at 950 K acquire 0.3 ± 0.01 and 1.75 ± 0.03 O-atoms/Mo, respectively. X-ray absorption edge energies in MoC_x-ZSM-5 increased from 0.2 to 1.9 eV (relative to Mo^0) after contact with 0.025 CO_2/CH_4 mixtures at 950 K for 1 h, indicating that oxidation of some Mo centers occurs. These spectral changes occurred concurrently with the detection of pre-edge features typical of MoO_x structures. Radial structure functions resemble those for samples exposed to pure CH_4, which consist of 0.6-nm MoC_x clusters, but show an additional Mo–O coordination shell also detected in bulk β-Mo_2C exposed to ambient air. These data suggest that the inhibition and ultimate suppression of catalytic pyrolysis reactions with CO_2 addition reflect the oxidation of active MoC_x structures, the extent of which increases with increasing CO_2/CH_4 reactant ratios. CO_2/CH_4 reactant ratios above 0.1 lead to conversion of MoC_x to MoO_x structures, which are inactive for both reforming and pyrolysis reactions of CH_4, but which reform active MoC_x after an induction period when exposed to pure CH_4 reactants at reaction conditions.

Keywords: Molybdenum; Carbides; ZSM-5; MFI; CO_2; CH_4; Reforming; Pyrolysis; EXAFS; XANES; Aromatization

1. Introduction

Medium-pore zeolites with MFI structure and modified by transition metal cations catalyze oligomerization, cyclization, and dehydrogenation reactions required to convert small alkanes to alkenes and arenes [1–14]. Wang et al. [15] first reported that MFI modification by contact with aqueous Mo^{6+} salts leads to near-equilibrium yields of ethene, ethane, and benzene during nonoxidative CH_4 reactions with low selectivities for larger unsaturated products, apparently because of steric constraints imposed by MFI channels. MoO_x precursors were shown to form carbide clusters during initial contact with CH_4 at 950 K [16]; these clusters provide the catalytic surfaces required for activation of C–H bonds in CH_4 and for removal of H-atoms as H_2 during both CH_4 conversion to C_2 molecules and sequential conversion of these primary C_2 products to arenes [17]. The exchange of acidic protons with D_2 [18], together with Raman spectroscopy and multiple-scattering simulations of the extended

* Corresponding author.
E-mail address: iglesia@cchem.berkeley.edu (E. Iglesia).

0021-9517/$ – see front matter
doi:10.1016/j.jcat.2004.11.037

fine structure in X-ray absorption spectra [19], provided direct evidence that Mo(VI)-oxo dimers form at exchange sites during sublimation of MoO_3/H-ZSM-5 physical mixtures. These Mo-oxo dimers subsequently convert to active MoC_x structures during CH_4 reactions.

Mo-ZSM-5 catalysts deactivate during nonoxidative CH_4 reactions [20–22] via carbon deposition processes, which become slower as external acid sites on zeolite crystals are selectively titrated by bulky organosilanes [23]. CO_2/CH_4 mixtures lead to slower deactivation than pure CH_4 reactants [24,25], an observation attributed to continuous carbon removal via

$$CO_2 + C^* \rightarrow 2CO + *. \quad (1)$$

A sudden loss of catalytic activity above a threshold CO_2/CH_4 reactant ratio (~ 0.06), reversed upon removal of CO_2 from the CH_4 reactant stream, has also been reported [26]. This sudden but reversible deactivation in CO_2/CH_4 feeds appears to reflect the oxidation of MoC_x instead of carbon deposition processes prevalent with pure CH_4 reactants [27]. At CO_2/CH_4 ratios below these threshold values, CH_4 conversion rates were lower but more stable than those obtained with pure CH_4 reactants. These lower rates reflect, at least in part, kinetic and thermodynamic inhibition by H_2 formed in CH_4–CO_2 reforming reactions; H_2 can also inhibit the formation of large organic residues. Lower pyrolysis rates may also reflect the continuous removal of reactive carbon, required for C–C bond formation, as CO, with the use of CO_2 as a reactant. Green et al. [28] examined CO_2 reforming on bulk Mo_2C and WC and proposed that CO_2 dissociates at carbon vacancies to form a steady-state concentration of chemisorbed oxygen (O*) at carbide surfaces. High O* thermodynamic activities, prevalent at high CO_2/CH_4 ratios, can lead to Mo_2C oxidation to less reactive MoO_x species.

Here we probe CH_4 pyrolysis catalysis and deactivation pathways on carburized $Mo_2O_5^{2+}$-ZSM-5 at low CO_2 concentrations by rigorously isolating and examining the kinetic and thermodynamic effects of CO_2 on measured reaction rates. Kinetic factors contributing to decreased hydrocarbon formation rates such as C* scavenging by CO_2 and H_2 and oxidative deactivation of carbide active sites are examined independently with varying feed composition and concentration. In contrast to previous studies, we report true forward rates by accounting for reactions of products and using thermodynamic equations that account for the equilibrium approach inherent in measured rates. Moreover, we report new evidence suggesting that the enhanced stability of Mo-ZSM-5 in CO_2/CH_4 mixtures is due to H_2 alone and not, as previously proposed, CO_2 [24]. Finally, in situ time-resolved mass spectrometry and X-ray absorption spectroscopy were used to measure the oxidation state, local coordination, and structure of Mo-ZSM-5 in CH_4 reactants with low CO_2 concentrations and to identify processes leading to the observed effects of CO_2 on the catalytic rates, selectivity, and ultimate reversible deactivation of active Mo-based structures at high CO_2 concentration.

2. Experimental

2.1. Catalyst synthesis

We prepared H-ZSM-5 from Na-ZSM-5 ($Si/Al_f = 20$, Zeochem; Al_f = framework Al) by heating Na-ZSM-5 (2 g) to 823 K at 0.083 $K\,s^{-1}$ in He (2.5 $cm^3\,s^{-1}\,g^{-1}$ Airgas, UHP) and holding at 823 K for 2 h in dry air (2.5 $cm^3\,s^{-1}\,g^{-1}$ Airgas, zero grade), a process that removes the organic templates used in ZSM-5 synthesis without a detectable loss of crystallinity. The resulting template-free Na-ZSM-5 (10 g) was converted to NH_4-ZSM-5 by ion exchange with 1 L of $NH_4NO_{3,aq}$ (1 M, Fisher, Cert. ACS) at 353 K for 12 h, followed by washing with 2 L of deionized H_2O. This exchange procedure was carried out three times with fresh solutions; samples were then dried for 12 h at 400 K in ambient air. NH_4-ZSM-5 (5 g) was converted to H-ZSM-5 by heating in 0.5 $cm^3\,s^{-1}\,g^{-1}$ dry air to 773 K at 0.167 $K\,s^{-1}$ and holding for 24 h. H-ZSM-5 and MoO_3 (Johnson Matthey, 99.5%) were then ground in an agate mortar and pestle for 0.2 h to form intimate mixtures containing a Mo/Al_f ratio of 0.41. This mixture was heated to 623 K at 0.167 $K\,s^{-1}$ and then held at 623 K for 24 h in 20% O_2/He to remove water and to spread MoO_3 on external zeolite surfaces [17,19]; finally, the mixture was heated to 973 K at 0.167 $K\,s^{-1}$ and held at 973 K for 2 h to form exchanged $Mo_2O_5^{2+}$-ZSM-5 [19]. The catalysts were formed into pellets with 0.12–0.25-mm diameter for use in structural characterization and catalytic studies.

2.2. Catalytic reactions of CH_4 and CH_4–CO_2 mixtures

Steady-state catalytic rates were measured at 950 K with 1-g catalyst samples held within a quartz reactor (12 mm i.d.). Reactants were 90% CH_4/Ar (Matheson, UHP, purified with a Matheson MTRP-0019-XX oxygen-moisture trap; 1 bar total pressure, 0.208 $cm^3\,s^{-1}$) mixed with 50% CO_2/He (Matheson, UHP) or H_2 (Airgas, UHP). We held CH_4 partial pressures constant (91 kPa) when using CO_2 or H_2 coreactants by increasing the total reactor pressure. The reactor effluent was directly transferred via heated lines (423 K) into a gas chromatograph (Agilent model 6890). Hydrocarbons were separated with a capillary column (Agilent HP-1, 50 m × 0.32 mm × 1.05 μm) and their concentrations were measured by flame ionization. CH_4, Ar, CO, CO_2, and H_2 were separated with a packed column (Agilent Porapak Q, 4.5 m) connected to a thermal conductivity detector. CH_4 conversion rates were measured with Ar as an internal standard to ensure rigorous mass balances. Product selectivities are reported on a carbon basis as the percentage of converted CH_4 molecules appearing as each product. Unreactive residues or nonvolatile products remaining on catalysts or transfer lines were determined by difference and reported as C_{12+}. CO selectivities are reported as the percentage of the CH_4 converted and appearing as CO (using half the total CO formed, i.e., excluding CO formed in Eq. (1)); in this way,

the sum of all reported carbon selectivities, including CO, equals unity. Yields are reported as the product of each selectivity and the fractional CH_4 conversion.

Measurements of O-atoms removed from or added to the catalyst with sudden changes in reactant composition required product analyses at short time intervals (< 1 s). Product evolution rates in these experiments were measured by mass spectrometry (MKS Minilab with electron multiplier; detection limit $\sim 1 \times 10^{-4}$ kPa for fixed gases), with the use of a heated capillary for continuous sampling of condensable species. All transient experiments were conducted at 950 K and ambient total pressure. During reduction/carburization of $Mo_2O_5^{2+}$-ZSM-5, the reactor feed was rapidly changed from pure He at 1 $cm^3\,s^{-1}$ to a mixture containing 54 kPa CH_4, 6 kPa Ar, and the balance in He at a total flow rate of 1 $cm^3\,s^{-1}$. During oxidation of reduced/carburized Mo-ZSM-5, the feed was switched from the latter composition to one containing 54 kPa CH_4, 6 kPa Ar, 1–3 kPa CO_2, and He as a balancing gas to maintain a constant flow of 1 $cm^3\,s^{-1}$. CH_4 pyrolysis and reforming products with overlapping mass fragments were measured with the use of matrix deconvolution methods adapted from earlier studies [18,29].

Measured net product formation rates are lower than the true kinetic forward rates when the product formed is involved in subsequent reactions or when reverse reactions become important near equilibrium. Forward rates, r_{forward}, corrected from the measured net reaction rates, r_{net}, in a sequential reaction (Eq. (2)) can be determined by correction for the approach to thermodynamic equilibrium with

$$CH_4 \xleftrightarrow{1} C_2H_4 \xleftrightarrow{2} C_6H_6 \xleftrightarrow{3} C_{10}H_8, \tag{2}$$

$$r_{C_2H_4,\text{forward}} = r_{C_2H_4,\text{net}} + r_{-1} + r_{C_6H_6,\text{net}} + r_{C_{10}H_8,\text{net}}, \tag{3}$$

$$r_{C_2H_4,\text{net}} + r_{-1} = r_{C_2H_4,\text{net}}/(1-\eta_1), \tag{4}$$

where the approach to equilibrium for reaction j, η_j (where $j = 1$ for ethene formation from methane), is given in terms of the partial pressures (in atm), p_i, of chemical species, i, and the equilibrium constant, K_j, for each reaction [30]

$$\eta_j = \frac{p_{C_2H_4}^{1/2} p_{H_2}}{p_{CH_4} K_j}. \tag{5}$$

2.3. Mo K-edge X-ray absorption spectroscopy

X-ray absorption spectra (XAS) were measured with the use of beamline 4-1 at the Stanford Synchrotron Radiation Laboratory (SSRL). Spectra were recorded in transmission mode with the use of three ionization chambers in series filled with a constant Ar flow. Catalyst samples were placed between the first two detectors, and a Mo foil (2.5 μm) was placed between the last two. The energy scale was calibrated from the first inflection point in the Mo foil K-edge (20 keV). The beamline was equipped with a Si(220) double-crystal monochromator and a downstream horizontal aperture (0.2 mm × 5.0 mm). Signal intensities were detuned to 70% of their maximum levels to minimize harmonic contributions. Spectra were acquired in 5-eV increments within the pre-edge region (19.80–19.98 keV), 0.25 eV near the edge (19.98–20.04 keV), and 0.04 $Å^{-1}$ in the fine structure region (3.24–16 k). Transient experiments required rapid scanning for accurate assessments of the dynamic evolution in the near-edge spectra (< 1 ks per spectrum). These rapid scans were measured in 5-eV increments from 19.85 to 19.98 keV, 0.5 eV from 19.98 to 20.03 keV, 3.77 eV from 20.03 to 20.13 keV, and 20.4 eV from 20.13 to 20.73 keV. The two types of spectral acquisition protocols described above are hereinafter denoted as methods 1 and 2.

The in situ X-ray absorption cell used in this study has been described previously [31,32]. Samples were held within a 0.8-mm i.d. quartz capillary with 0.1-mm-thick walls. Gases were metered with electronic mass flow controllers in a manifold capable of producing streams prepared from three different gas sources. H-ZSM-5 was exchanged with MoO_3 with the procedures described above, before X-ray absorption measurements were recorded. $Mo_2O_5^{2+}$-ZSM-5 was exposed to 90% CH_4/Ar (Praxair, UHP) at 950 K, and reduction and carburization processes were monitored from X-ray absorption near-edge spectra (XANES) with acquisition method 2; we determined the extent of carburization by monitoring changes in the pre-edge absorption feature. When the pre-edge features became undetectable, samples were exposed to one of two reaction mixtures. Some samples were exposed to pure CH_4 for 1 h, and then extended X-ray absorption fine spectra (EXAFS) were recorded with method 1. The remaining samples were exposed to a reaction mixture with a 0.025 CO_2/CH_4 molar ratio and the XANES region was monitored with acquisition method 2 until no further spectral changes were detected, at which time a detailed spectrum, including the details of the fine structure, was acquired with method 1.

MoO_3 (Johnson Matthey, 99.5%), MoO_2 (Aldrich, 99.9%), β-Mo_2C (prepared by temperature-programmed reduction of MoO_3 in 20% H_2/CH_4 at 973 K [33]), $MgMo_2O_7$ (prepared as in [34]), and $(NH_4)_2Mo_2O_7$ (Strem Chemicals, 99.98%) were diluted with boron nitride and sealed with Kapton tape before we acquired X-ray absorption spectra for these materials with known structures. The β-Mo_2C sample was passivated before exposure to ambient air; the near-surface regions of the sample contained oxygen. These compounds provide structural and oxidation state standards for the assessment of unknown structures as they evolve during catalysis in various reactant mixtures.

Spectra were analyzed with the use of WinXAS Version 2.1 [35]. Pre-edge and post-edge baselines were subtracted with the use of first- and third-order polynomials, respectively, and the near-edge region was analyzed between 19.90 and 20.12 keV. The absorption background was removed and k^2-weighted spectra were transformed between 2.6 and 13.0 $Å^{-1}$. The spectra were then corrected for phase shift and fitted in R-space between 0.5 and 4 Å with the use of the Hanning window and FEFFIT [36] to determine interatomic

distances and coordination numbers. Backscattering amplitudes and phase shifts of theoretical standards were generated with the use of FEFF8.0 [37] algorithms, and ATOMS [38] was used to generate the required input files from previously reported atomic coordinates. We determined the amplitude reduction factor, S_0^2, by fitting experimental Mo foil spectra. Factor analysis was used to identify the principal components in the samples from near-edge spectra recorded during transient experiments. WinXAS software contains a built-in factor analysis code that uses the Malinowski indicator function [39] to estimate the number of pure components, and a target transformation module to identify the pure components [40]. The target transformation algorithm generates an absorption vector of a known reference compound by interpolating its spectra onto the same energy grid as the unknown experimental spectra. A least-squares fitting procedure is then used to determine a transformation vector that will be identical to the absorption vector of the reference compound within experimental error if the reference is indeed a principal component. A goodness-of-fit parameter, or residual, less than 1% is generally considered acceptable [40].

3. Results and discussion

3.1. Steady-state catalytic studies

Steady-state catalytic rates and selectivities were first measured on $Mo_2O_5^{2+}$-ZSM-5 ($Mo/Al_f = 0.41$) at 950 K with the use of pure CH_4 reactants (91 kPa). This catalyst composition led to maximum CH_4 pyrolysis rates by balancing the number of MoC_x species required for CH_4 activation and the residual Brønsted acid sites required for alkene oligomerization and cyclization, while avoiding dealumination of the zeolite framework via formation of Al molybdate species at higher Mo loadings [17].

Table 1 shows forward rates for product formation at 950 K and 91 kPa CH_4 after 8.6 and 30.1 ks of contact with reactants. Ethane and ethene η values are almost identical, indicating that their interconversion is equilibrated. The approach to equilibrium for arene synthesis was substantial but decreased with time because of catalyst deactivation by deposition of unreactive residues, which form on active sites within channels, restrict reactant access to such sites, and decrease CH_4 conversion levels [27]. The sequential nature of arene formation pathways (via C_2 initial products) led to stronger time-on-stream effects on arene formation rates than on C_2 formation rates. Thus, the selectivity shifts to primary C_2 products as deactivation occurs.

CO_2 was added to CH_4 reactants to probe the effects of CO_2 concentration on CH_4 reaction rates and catalyst stability. Steady-state CH_4 conversion and CO and hydrocarbon yields are shown in Fig. 1 for CO_2/CH_4 molar ratios less than 0.1. Samples were first activated by reduction and carburization with pure CH_4 reactants until hydrocarbon yields

Table 1
CH_4 pyrolysis over Mo/H-ZSM-5 (1 g, $Mo/Al_f = 0.41$, 950 K, 0.19 $cm^3\ s^{-1}$ CH_4; 101.1 kPa, CH_4:Ar = 9:1)

Time on stream (ks)	8.6	30.1
CH_4 conversion (%)	7.0	4.8
Distance to equilibrium (η, %)[a]		
C_2H_4	87	70
C_2H_6	86	71
C_6H_6	54	25
C_7H_8	57	29
$C_{10}H_8$ (naphthalene)	44	19
Forward rates (10^{-3} mol/(g-atom Mo-s))		
C_2	2.04	1.17
C_6H_6	2.55	1.16
C_7H_8	0.14	0.09
$C_{10}H_8$	0.47	0.15
Selectivity (% carbon)		
C_2H_4	3	7
C_2H_6	2	3
C_6H_6	54	59
C_7H_8	3	5
$C_{10}H_8$	14	9

[a] η, Distance to equilibrium for each product defined in Eqs. (2)–(5) (Section 2.2).

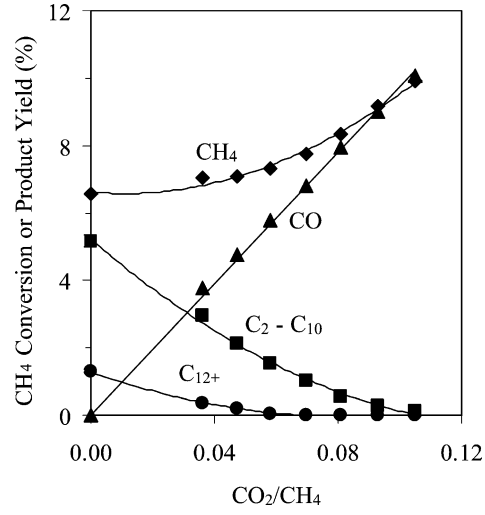

Fig. 1. CH_4 conversion and hydrocarbon yield as a function of CO_2/CH_4 ratio on Mo/H-ZSM-5 (1 g, $Mo/Al_f = 0.41$, 950 K, 0.19 $cm^3\ s^{-1}$ CH_4, 91 kPa CH_4).

reached maximum values ($\sim$ 2 h); CO_2 was then added. CH_4 conversion remained constant at $\sim$ 7% for CO_2/CH_4 ratios below 0.064; CO_2 was not detected in the effluent with these reactant mixtures. At slightly higher CO_2/CH_4 ratios, CH_4 conversion increased proportionally with CO_2 concentration. Methane conversions were very similar to the sum of hydrocarbons and CO (from CH_4, defined in the Experimental section) yields; no detectable C_{12+} products were formed at these moderate CO_2 concentrations. Fig. 2 shows CH_4 conversion and hydrocarbon and CO yields for reactant mixtures with CO_2/CH_4 ratios of 0, 0.05, and 0.1 after activation in pure CH_4 for 2 h. Hydrocarbon yields were 2.1% at a 0.05 CO_2/CH_4 ratio and did not decrease even

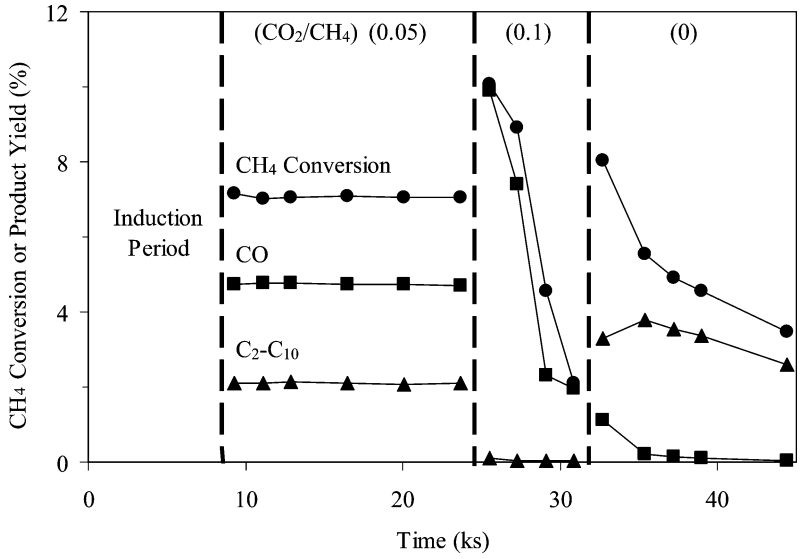

Fig. 2. CH_4 conversion and hydrocarbon yield as a function of time on Mo/H-ZSM-5 (1 g, $Mo/Al_f = 0.41$, 950 K, 0.19 $cm^3\,s^{-1}$ CH_4, 91 kPa CH_4).

after 15 ks; only traces of C_{12+} hydrocarbons were formed. At a CO_2/CH_4 ratio of 0.1, the initial CH_4 conversion was $\sim$ 10%, CO_2 was completely consumed within the catalyst bed, and hydrocarbons were virtually undetected at less than two orders of magnitude of their yields in CO_2 free feeds (Fig. 2, right panel). With this reactant mixture, CH_4 conversion decreased abruptly to undetectable levels after $\sim$ 1 h. Removal of CO_2 from the reactant stream led to the recovery of catalytic rates, after an activation period of 3 ks, during which CO was formed and hydrocarbons increased to maximum rates (Fig. 2, right panel).

The lower hydrocarbon yields obtained with CO_2 coreactants may reflect thermodynamic or kinetic effects. H_2 formed via CH_4–CO_2 reforming would decrease equilibrium CH_4 conversion levels and increase rates for the reverse of the dehydrogenation steps required to form alkenes and arenes. Adsorbed organic species may be removed continuously by CO_2, thus inhibiting chain growth processes requiring C–C bond formation, but ultimately replacing carbidic carbon in MoC_x with O-atoms until CO_2 is depleted along the catalyst bed. CO products of CH_4–CO_2 mixtures may also form unreactive carbon species via Boudouard reactions that impede access to active sites. We consider each of these possible effects below.

Net rates were corrected for approach to equilibrium to assess the role of H_2 formed in CH_4–CO_2 reactions on pyrolysis forward rates. The resulting (forward) arene synthesis rates decreased with increasing CO_2 concentration (Fig. 3). Equilibrium calculations for combined pyrolysis and CO_2 reforming reactions, made with thermodynamic data [41,42], showed that net hydrocarbon yields decreased with increasing CO_2 feed concentration because of the H_2 formed in CO_2 reforming reactions. If H_2 were solely responsible, however, for the observed effects of CO_2 on hydrocarbon synthesis rates, forward arene synthesis rates would be independent of CO_2 concentration, in contradiction to the data shown in Fig. 3.

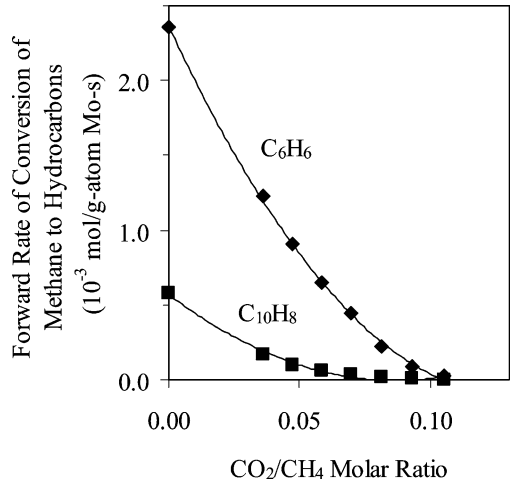

Fig. 3. Forward product synthesis rates as a function of CO_2/CH_4 ratio on Mo/H-ZSM-5 (1 g, $Mo/Al_f = 0.41$, 950 K, 0.19 $cm^3\,s^{-1}$ CH_4, 91 kPa CH_4).

We next consider the effect of H_2 on pyrolysis rates independently of CO_2 with H_2/CH_4 reactants. H_2 can decrease net arene synthesis rates because of thermodynamic effects, which are accounted for through our use of forward rates, or via scavenging of reactive carbon and suppression of C–C bond formation pathways. Fig. 4a shows benzene forward rates as a function of average H_2 pressure (defined as the mean of its inlet and outlet values) with both H_2/CH_4 and CO_2/CH_4 reactants (at 950 K and 91 kPa CH_4). We calculated inlet H_2 pressures for CO_2/CH_4 mixtures by assuming that CO_2 is depleted near the bed inlet and H_2 forms with the stoichiometry of CH_4–CO_2 reactions. Forward rates of benzene synthesis decreased with increasing H_2 pressure in H_2/CH_4 feeds, indicating that H_2 kinetically inhibits CH_4

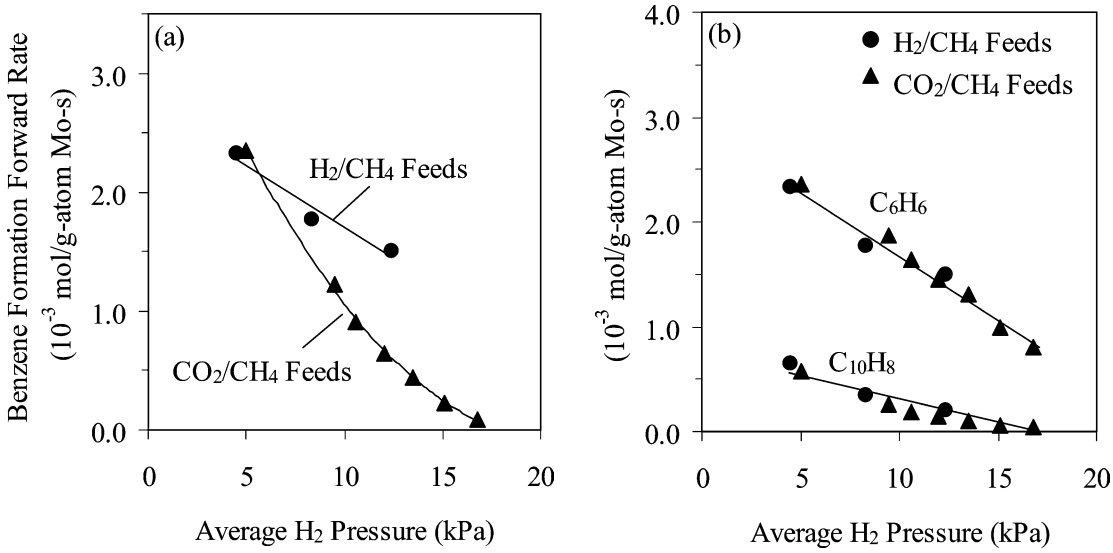

Fig. 4. Forward benzene formation rate as a function of average H_2 pressure on Mo/H-ZSM-5 (1 g, $Mo/Al_f = 0.41$, 950 K, 0.19 $cm^3\ s^{-1}$ CH_4, 91 kPa CH_4) assuming (a) CO_2 is completely consumed near bed inlet and (b) CO_2 is consumed at an intermediate point along the bed proportional to the CO_2 inlet concentration given by Eqs. (6) and (7). The average H_2 pressure is defined as the arithmetic mean of the inlet and outlet H_2 partial pressures. The inlet H_2 partial pressure for CO_2/CH_4 mixtures is defined as the partial pressure of H_2 produced in CO_2 reforming reactions.

pyrolysis reactions, because we take thermodynamic effects into account by using Eqs. (2)–(5) to calculate forward rates. Benzene synthesis forward rates were always higher with H_2/CH_4 than with CO_2/CH_4 reactants for any given average H_2 pressure. Therefore, the lower benzene forward rates observed with CO_2/CH_4 mixtures are not caused only by inhibition by the H_2 formed (in CH_4–CO_2 reforming reactions) near the bed inlet.

The data in Fig. 2 show that at CO_2 conversions below 100%, hydrocarbon yields decrease by two orders of magnitude compared with those with CO_2-free feeds. CO_2 scavenges C* before C–C bond formation can occur, thus preventing pyrolysis reactions at any reactor position that contains unreacted CO_2. Thus, the fraction of the catalyst bed that remains available for CH_4 pyrolysis reactions decreases with increasing CO_2 concentration. CO_2 reforming rates on Ni and noble metal catalysts have been shown to be independent of CO_2 and proportional to CH_4 concentrations [43,44]; therefore, the fraction of the catalyst exposed to CO_2 should be proportional to the inlet CO_2 concentration at these low CO_2/CH_4 ratios. Forward pyrolysis rates (Fig. 4a) thus reflect only that part of the bed remaining after CO_2 depletion. We account for this smaller amount of active catalyst by using the CO_2 concentration where no hydrocarbons are detected as the threshold CO_2 concentration, C_{max}, and assuming that for feeds with CO_2 inlet concentration, C_i, the CO_2 is completely consumed at a bed length, L_i, equal to

$$L_i = (LC_i)/C_{max}, \tag{6}$$

where L is the length of the fixed-bed reactor. Forward rates corrected for effective bed length are then equal to

$$r_{forward,eff} = \frac{r_{forward}}{1 - L_i/L}. \tag{7}$$

The $r_{forward,eff}$ vs average H_2 partial pressure is plotted in Fig. 4b. Benzene forward rates for H_2/CH_4 and CO_2/CH_4 feeds collapse onto a single line, confirming our new model for the complete suppression of pyrolysis reactions by CO_2. Naphthalene synthesis rates for CO_2/CH_4 and H_2/CH_4 feeds also lie along the same line.

The effective forward rates in Fig. 4 suggest that the lower pyrolysis yields with CO_2/CH_4 mixtures occur as a result of a shorter active catalyst bed available for pyrolysis as a result of CO_2 scavenging of active C* near the bed inlet. Yet we observe, as have others [24], that pyrolysis rates are much more stable with time on stream when CO_2 is present in CH_4 feeds, even though pyrolysis occurs only in those regions of the bed where CO_2 is no longer present. Such regions of the bed can detect the presence of CO_2 in the inlet stream only through the presence of the H_2 and CO products formed in CH_4–CO_2 reactions. First-order deactivation constants for hydrocarbon synthesis were 0.011 and 0.0008 ks^{-1}, with CH_4 (5 kPa average H_2 pressure $\langle H_2 \rangle$) and 0.06 CO_2/CH_4 (12.5 kPa $\langle H_2 \rangle$) feeds, respectively, as shown in Table 2. For a H_2/CH_4 feed with an average H_2 pressure (12 kPa $\langle H_2 \rangle$) similar to that prevalent after CO_2 depletion with 0.06 CO_2/CH_4 reactants, the deactivation constant was 0.001 ks^{-1}, a value very similar to that obtained with CO_2 coreactants (0.0008 ks^{-1}). The similar deactivation constants for feeds with similar average H_2 pressures (12–12.5 kPa) but different inlet compositions confirm that the sole effect of CO_2 coreactants on deactivation is to form H_2, which acts as the deactivation inhibitor in downstream pyrolysis reactions of the catalyst bed, within which CO_2 could not have any more direct effects because it is no longer available. This exclusive role of H_2 in inhibiting deactivation processes contrasts with previous claims attributing it

Table 2
First order deactivation constants and benzene forward rates over Mo-ZSM-5 (1 g, $Mo/Al_f = 0.41$, 950 K, 0.19 $cm^3\ s^{-1}$ CH_4, 91 kPa CH_4) with different average H_2 partial pressures

Average H_2 pressure of feed mixture (kPa)	k_d (10^{-2} ks^{-1})			Benzene rate (10^{-3} mol/(g-atom Mo-s))		
	CH_4	H_2/CH_4	CO_2/CH_4	CH_4	H_2/CH_4	CO_2/CH_4[a]
5	1.10	–	–	2.35	–	–
12	–	0.10	–	–	1.50	–
12.5	–	–	0.08	–	–	1.45

[a] Benzene forward rate corrected for effective bed used for pyrolysis (Eqs. (6) and (7)).

directly to CO_2 scavenging of C* via reverse Boudouard reactions [24].

Forward rates measured as a function of inlet composition indicate that the catalyst bed can be described as two discrete sections, catalyzing reforming and pyrolysis reactions, at low CO_2/CH_4 ratios. Pyrolysis does not occur while CO_2 is available because it effectively scavenges C* intermediates required for chain growth. The downstream pyrolysis section acts as a catalyst bed with an inlet stream containing CH_4 and equimolar amounts of H_2 and CO. The shorter effective bed for pyrolysis and the thermodynamic effects of H_2 formed in the reforming section lead to lower hydrocarbon yields than with pure CH_4 inlet streams, but also to lower deactivation rates as a result of the role of H_2 in preventing the formation of unreactive residues, probably large polynuclear aromatics requiring sequential dehydrogenation steps reversed by H_2.

The active Mo phase within pyrolysis sections of the bed consists of small carbide clusters similar to Mo_2C [16,45], but the structure and oxidation state of the section of the bed exposed to CO_2 remain unclear. In the sections that follow, we explore the structural and catalytic consequences of CO_2/CH_4 mixtures by mass spectrometric analysis of the bed effluent during compositional transients and in situ X-ray absorption spectroscopy to provide evidence that oxidation of Mo carbides at high CO_2 concentrations forms a Mo phase that is inactive for C–H bond breaking and therefore for catalytic pyrolysis of CH_4.

3.2. Transient evolution of products during contact with CO_2/CH_4 reactant mixtures

The removal of C* by CO_2 to form CO and the potential replacement of the C* species in MoC_x by oxygen to form MoO_x species inactive in pyrolysis and even reforming reactions may account for the deactivation of Mo-ZSM-5 observed at high CO_2 concentrations (Fig. 2). The resulting depletion of reactive C* (or CH_x*) monomers would prevent C–C bond formation within regions in the reactor containing CO_2. We examined these effects by measuring changes in effluent composition, as inlet CO_2 concentrations were abruptly changed in an effort to measure the number of O atoms added to or removed from working catalysts in environments containing different CO_2 concentrations.

Fig. 5a shows the CO, H_2O, H_2, C_2H_4, and C_6H_6 formation rates and CH_4 conversion during initial contact of $Mo_2O_5^{2+}$-ZSM-5 with CH_4 at 950 K. H_2, H_2O, and CO were initially detected as a result of the reduction and carburization of trace amounts of unexchanged MoO_3 [29]; these products inhibit the reduction and carburization of less reducible exchanged Mo-oxo dimers. As these dimers ultimately converted to MoC_x clusters, H_2O concentrations decreased and H_2 and CO formation rates increased sharply until all of the O atoms in $Mo_2O_5^{2+}$ were removed and catalysts reached maximum CH_4 pyrolysis rates. Initial exposure of $Mo_2O_5^{2+}$-ZSM-5 to CH_4 ($CO_2/CH_4 = 0$; Fig. 5a) removed 2.5 ± 0.05 O atoms per Mo atom (Fig. 6, left panel), measured from the concentration of oxygen-containing products (CO, CO_2 ($x2$), H_2O), indicating that all nonzeolitic O atoms in exchanged $Mo_2O_5^{2+}$ were removed, as shown previously [18]. Benzene, a representative pyrolysis product, was first detected at ~ 500 s (Fig. 5a) and reached maximum synthesis rates (5×10^{-4} mol/(g-atom Mo-s)) before decreasing gradually as deactivation occurred.

Next we consider the transient behavior of $Mo_2O_5^{2+}$-ZSM-5 samples first carburized in pure CH_4 (for 1 h) and then exposed to reactants with a CO_2/CH_4 molar ratio of 0.022 (Fig. 5b). During initial carburization and catalytic CH_4 pyrolysis, CH_4 conversion decreased to $\sim 1\%$ after 1 h before CO_2 was introduced into the pure CH_4 stream. CO_2 was completely converted and CH_4 conversion increased immediately to $\sim 3\%$ upon the introduction of CO_2. The CH_4 conversion oscillations in Fig. 5b reflect pumping fluctuations in the mass spectrometer; they occurred in this experiment also before CO_2 addition and do not reflect oscillations in catalytic rates. Measured net benzene synthesis rates decreased from 2×10^{-4} to 5×10^{-5} mol/(g-atom Mo-s) during CO_2 addition.

We measured the amount of oxygen introduced into this sample during contact with this CO_2-containing reactant mixture by subtracting the CO formed from the amount of CO required for CO_2 reforming of CH_4. H_2O, which forms in concurrent water–gas-shift reactions, was below the detection limit, as expected from water–gas shift equilibrium calculations under these reaction conditions ($\sim 10^{-9}$ kPa). CO_2/CH_4 inlet ratios of 0.022 and 0.055 led to the introduction of 0.28 ± 0.01 and 1.8 ± 0.03 O atoms per Mo atom (Fig. 6, middle panel), respectively, into MoC_x clusters formed during initial contact with pure CH_4 reactants. This suggests that some C* in MoC_x is replaced with O* at the beginning of the bed where CO_2 was present, but the catalyst bed remains active for CO_2 reforming and CH_4 pyrolysis

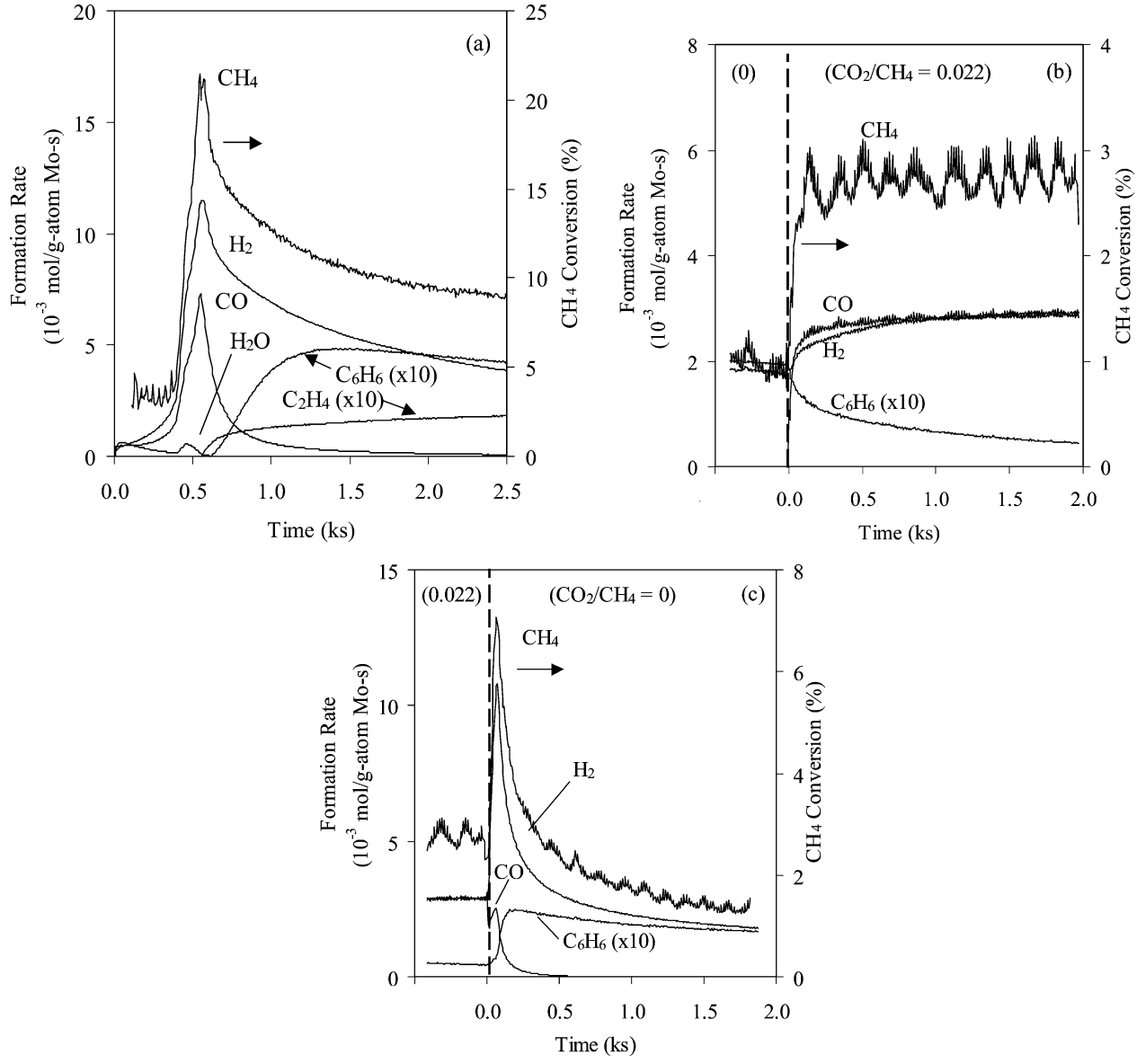

Fig. 5. Transient product formation rates and CH_4 conversion during reactions of CO_2/CH_4 mixtures on Mo/H-ZSM-5 (1 g, $Mo/Al_f = 0.41$, 950 K, 1 $cm^3\ s^{-1}$, 54 kPa CH_4) (a) $CO_2/CH_4 = 0$, (b) 0.022 CO_2/CH_4, and (c) $CO_2/CH_4 = 0$ after (b).

at these CO_2 concentrations. Fig. 5c shows product evolution profiles after a 0.022 CO_2/CH_4 stream was replaced with pure CH_4 reactants. CH_4 conversion increased sharply to 7%, and then benzene synthesis rates gradually returned to the values measured during initial contact with pure CH_4 reactants ($\sim 2 \times 10^{-4}$ mol/(g-atom Mo-s)) in ~ 1 ks. The number of O atoms removed during exposure to pure CH_4 reactants was measured from the number of CO molecules formed during contact with pure CH_4 reactants (only traces of H_2O and CO_2 formed) (Fig. 6, right panel). This procedure yielded 0.31 ± 0.01 and 1.7 ± 0.03 O atoms removed per Mo atom for CO_2/CH_4 ratios of 0.022 and 0.055, respectively (Table 3). These values are consistent with the amounts of oxygen deposited on active oxygen-free MoC_x structures during contact with each of these CO_2-containing streams (0.28 and 1.8 O/Mo, respectively).

After CO_2 was removed from the inlet stream, benzene synthesis rates returned to values measured before CO_2 introduction, but not to those measured after initial activation of fresh exchanged samples in pure CH_4 streams. The formation of carbon deposits on acid sites and external surfaces has been examined by X-ray photoelectron spectroscopy and reactivity studies [27,46]; unreactive carbon residues restrict channel entrances, and their formation is essentially irreversible, except by treatment in O_2 at high temperatures [17]. Oxidation of MoC_x-ZSM-5 in O_2 at 973 K restores more than 90% of initial pyrolysis rates [17] by converting deactivated MoC_x clusters to MoO_3 and redispersing it as $Mo_2O_5^{2+}$ dimers above 623 K. In contrast, MoC_x oxidation in CO_2/CH_4 reactant mixtures does not remove unreactive carbon deposits formed during pyrolysis at other locations, even though these mixtures led to significant conversion of

Table 3
O-atom addition/removal from $Mo_2O_5^{2+}$-ZSM-5 (1 g, $Mo/Al_f = 0.41$, 950 K, 1 $cm^3\,s^{-1}$; 54 kPa CH_4, 6 kPa Ar, balance He with 101.3 kPa total)

CO_2/CH_4	(O-atoms) removed/Mo		
	During initial contact $Mo_2O_5^{2+}$ with CH_4	After carburization and introduction of CO_2/CH_4	After reintroduction of CH_4
0.022	+2.6	−0.28	+0.31
0.055	+2.5	−1.8	+1.7

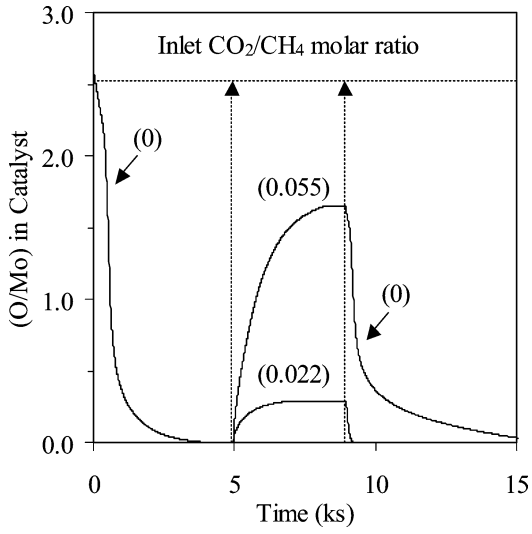

Fig. 6. (O/Mo) in catalyst as a function of time on Mo/H-ZSM-5 (1 g, $Mo/Al_f = 0.41$, 950 K, 1 $cm^3\,s^{-1}$, 54 kPa CH_4). Numbers in parenthesis denote CO_2/CH_4 ratio in feed.

MoC_x species to the corresponding suboxides. The formation of these unreactive deposits appears to be inhibited in CO_2-containing feeds, as shown by the low deactivation rates observed for reactant mixtures with CO_2/CH_4 ratios below 0.1, which reflect the presence of H_2 formed via CO_2 reforming near the bed inlet. CO_2 addition did lead to the ultimate replacement of chemisorbed carbon with oxygen as illustrated in Fig. 7. Fig. 7 depicts a Mo_2C particle formed during activation processes in CH_4 described above and suddenly exposed to a CO_2/CH_4 reactant mixture. CO_2 can react directly with a vacancy to form CO and O*, or it can react with a surface C* to form two CO molecules and a vacancy (as in Eq. (1)). Similar oxidative deactivation pathways on bulk and supported Mo_2C and WC during CO_2 reforming of CH_4 were proposed by Green et al. [28]. O atoms, generated by dissociation of CO_2, react with carbon in carbide structures to form a carbon vacancy that can then be filled with additional O atoms from CO_2, leading to the ultimate oxidation of MoC_x structures. Such vacancies can react also with C* formed via CH_4 dissociation to reform a stoichiometric carbide; these processes are in a state of dynamic balance during steady catalysis, as depicted in Fig. 7.

These conclusions about reduction–carburization–oxidation cycles are based on rigorous chemical balancing of inlet and outlet streams; they do not, however, provide direct evidence for structural changes in Mo centers during contact with reactant streams with different CO_2/CH_4 ratios. In the following section, we describe catalyst structure and electronic properties with the use of near-edge (XANES) and extended fine structure (EXAFS) analysis of X-ray absorption spectra during catalytic reactions of CH_4–CO_2 mixtures.

3.3. *In situ near-edge and fine structure X-ray absorption spectra at the Mo K-edge*

Near-edge X-ray absorption spectra are shown in Fig. 8 for exchanged $Mo_2O_5^{2+}$-ZSM-5 prepared from MoO_3/H-ZSM-5 physical mixtures and for reference Mo compounds with known structure. The spectra for the initial physical mixtures resembled that for crystalline MoO_3, within which Mo atoms reside in distorted octahedral coordination. Thermal treatment to 950 K in 20% O_2/He led to gradual changes in the near-edge spectra of these mixtures. The spectra ul-

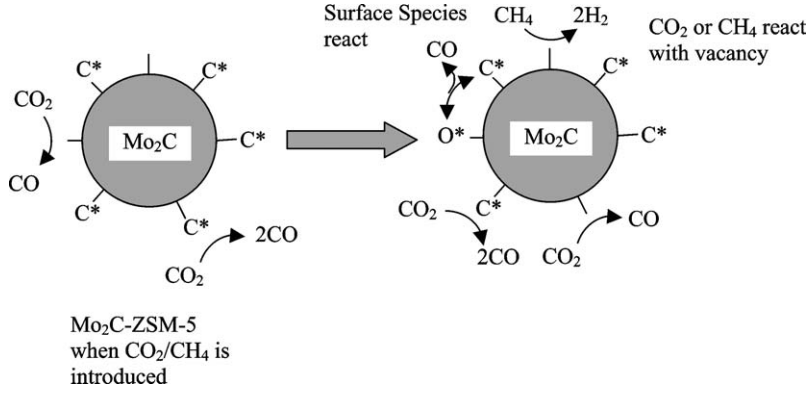

Fig. 7. Schematic representation of MoC_x-ZSM-5 surface in CO_2/CH_4 ($\ll 1$) reactant mixtures. The left cluster depicts initial exposure of Mo_2C to CO_2/CH_4, and the right cluster depicts reactions involving surface species and gaseous CH_4 and CO_2.

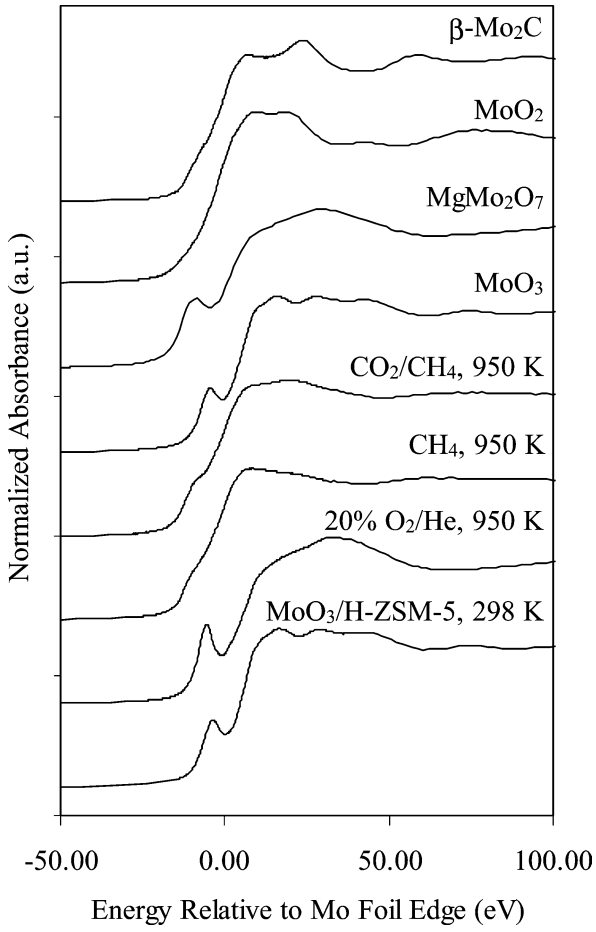

Fig. 8. Mo K-edge near-edge spectra for β-Mo_2C exposed to air, MoO_2, $MgMo_2O_7$, MoO_3 and physical mixtures of MoO_3/H-ZSM-5 ($Mo/Al_f = 0.41$) during treatment in 20% O_2/He at 298 and 950 K, CH_4 at 950 K and $CO_2/CH_4 = 0.025$ at 950 K.

Table 4
Edge energy position of Mo (relative to Mo foil edge at 20,000 eV) in reference compounds and Mo/H-ZSM-5

Compound	ΔE_0 (eV)
MoO_3	4.8
β-Mo_2C	0.2
$(NH_4)_2Mo_2O_7$	4.4
MoO_3/H-ZSM-5	4.3
$Mo_2O_5^{2+}$-ZSM-5	4.9
$Mo_2O_5^{2+}$-ZSM-5 after treatment in CH_4 at 950 K for 1 h	0.2
$Mo_2O_5^{2+}$-ZSM-5 after treatment in CH_4 at 950 K for 1 h then in $CO_2/CH_4 = 0.025$ at 950 K for 1 h	1.9

timately resemble that for $MgMo_2O_7$, which contains ditetrahedral Mo centers, indicating the presence of $Mo_2O_5^{2+}$-ZSM-5 structures anchored at vicinal exchange sites [19]. $Mo_2O_5^{2+}$-ZSM-5 exhibits a pre-edge feature, which arises from $1s \rightarrow 4d$ electronic transitions; these transitions are dipole-forbidden for centrosymmetric Mo centers. As electrons are placed in $4d$ orbitals during reduction of Mo^{6+} cations, these transitions become less probable and pre-edge features become weaker and ultimately undetectable in Mo^0 [19,47,48]. MoO_2 contains partially filled $4d$ shells and does not show a pre-edge feature. $Mo_2O_5^{2+}$-ZSM-5 has a more intense pre-edge feature (Fig. 8) than MoO_3, indicating a change in Mo coordination from distorted octahedral to tetrahedral during thermal treatments leading to exchange [49,50]. Pre-edge features in $Mo_2O_5^{2+}$-ZSM-5 disappeared upon contact with CH_4 at 950 K for 1 h, indicating that Mo-oxo species reduced and carburized during catalysis. Subsequent exposure of MoC_x structures to reactants with CO_2/CH_4 ratios of 0.025 for 1 h led to the reappearance of pre-edge features, albeit with much lower intensity than in fresh exchanged $Mo_2O_5^{2+}$-ZSM-5.

Changes in the absorption edge energy were also detected during catalytic reactions with other CO_2/CH_4 reactant mixtures (Table 4). The edge energy was taken as the first inflection point in the absorption edge (or the first inflection after the pre-edge feature, if present). Fresh exchanged $Mo_2O_5^{2+}$-ZSM-5 showed an edge energy (relative to Mo^0) at 4.90 eV, similar to that of MoO_3 (4.8 eV) and corresponding to that of Mo^{6+}. After exposure to CH_4, the edge shifts to 0.2 eV and then back to 1.9 eV after contact with a 0.025 CO_2/CH_4 mixture at 950 K for 1 h. These data show that reduction and carburization occur during activation in pure CH_4 and that these processes are reversed, to some extent, as CO_2 is introduced along with CH_4 reactants. As CO_2 is depleted along the plug-flow reactor cell, the composition of the gas phase changes, leading to a mixture of Mo structures and oxidation states, all of which are sampled by the X-ray beam during these absorption measurements.

Factor analysis was used to identify principal components from near-edge spectra. This method has been used previously to identify pure components contributing to X-ray absorption spectra [40,49,51,52]. First, factor analysis was used to determine that two principal components contributed to the 11 near-edge spectra acquired during transient $CO_2/CH_4 = 0.025$ addition. The identities of pure components in CO_2/CH_4 feed transients were established with the use of a target transformation algorithm in WinXAS 2.1 (see details in the Experimental section). $Mo_2O_5^{2+}$-ZSM-5 treated in CH_4 for 1–6 h in CH_4 at 950 K was shown to exist as 0.5–0.6 nm Mo_2C clusters from multiple-scattering simulations of the absorption fine structure [19,45]. MoC_x was identified as a principal component with a residual of 0.26% in carburized Mo-ZSM-5 in this study; residuals lower than 1% indicate an unequivocal identification of a principal component [40]. The fresh exchanged $Mo_2O_5^{2+}$-ZSM-5 sample gave a residual of 5%, a relatively poor fit compared with the carburized Mo-ZSM-5 structural standard. Bulk MoO_3 gave a residual of 2.6%, considerably better than $Mo_2O_5^{2+}$-ZSM-5, but still high. Oxycarbides, as depicted in Fig. 7, are most likely the dominant species at 0.025 CO_2/CH_4, and therefore neither one of the reference compounds accurately describes the experimental transient spectra. In lieu of suitable standards, the oxidation of active Mo carbides by CO_2/CH_4 mixtures can be described by two principal com-

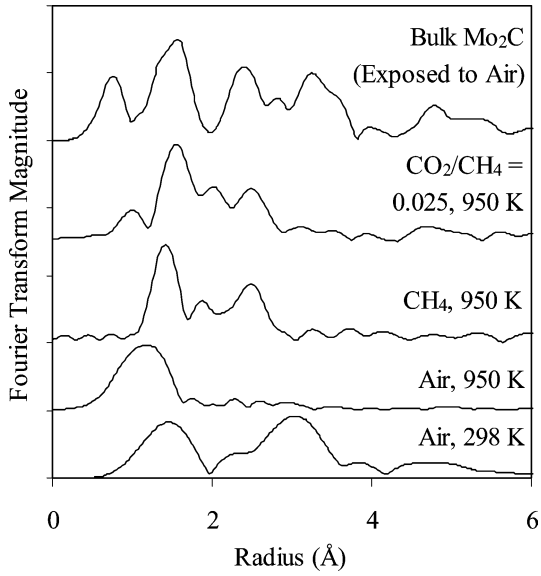

Fig. 9. Radial structure function (RSF) for β-Mo_2C exposed to air and for MoO_3/H-ZSM-5 ($Mo/Al_f = 0.41$) during treatment in 20% O_2/He at 298 and 950 K, CH_4 at 950 K and $CO_2/CH_4 = 0.025$ at 950 K. RSF for each sample was generated by Fourier-transform magnitude of k^2-weighted EXAFS.

ponents, one of which is Mo_2C, but the identification of the other principal components remains ambiguous at this time.

A Fourier transform of the fine structure region gives a radial structure function around Mo absorbers (e.g., Fig. 9 for $Mo_2O_5^{2+}$-ZSM-5). The intensity of the features is related to the number of scatterers at a given distance from Mo atoms, which is corrected in structural fits by thermal and static disorder and by the scattering cross section of the neighboring atoms. Fig. 10 shows experimental and fitted k^2-weighted EXAFS and radial scattering functions for $Mo_2O_5^{2+}$-ZSM-5; the parameters arising from structural refinement procedures are shown in Table 5. These fine structure spectra for exchanged $Mo_2O_5^{2+}$-ZSM-5 in 20% O_2/He were described via multiple scattering simulations with $MgMo_2O_7$ standards as the starting point. The resulting simulated structures confirmed that each Mo atom has four oxygen neighbors in a tetrahedral arrangement at a distance of 0.16–0.18 nm. Scattering from next-nearest neighboring Mo or Al was not detected in the experiments or in simulated radial structure functions because of a π phase shift in multiple scattering paths, which leads to destructive interference of scattered electrons [19].

Several features emerged in the radial structure function of $Mo_2O_5^{2+}$-ZSM-5 upon exposure to CH_4 at 950 K for 1 h (Fig. 10). These features can be described with the use of a cluster with three Mo–C shells and a total coordination of 3.4 together with a weak contribution from a Mo–Mo shell at 0.29 nm with a coordination number of 0.3. A new feature near 0.12 nm appeared in the radial structure function after exposure to CO_2/CH_4 mixtures at 950 K for 1 h (Fig. 10), but the sample otherwise retained the features present in the sample during contact with pure CH_4 reactants. The feature at 0.12 nm and the rest of the radial structure function resemble those in bulk Mo_2C containing some oxygen coordination as a result of exposure to ambient air (Fig. 9). The new feature at 0.12 nm was fitted with a Mo–O shell at 0.17 nm with a coordination number of 0.2. Only two Mo–C shells were needed to describe the structure; this gave an overall Mo–C coordination of 3.4. The Mo-ZSM-5 catalysts in CH_4 and CO_2–CH_4 lack scattering centers at longer distances, which is typical of the bulk carbide (Fig. 9), sug-

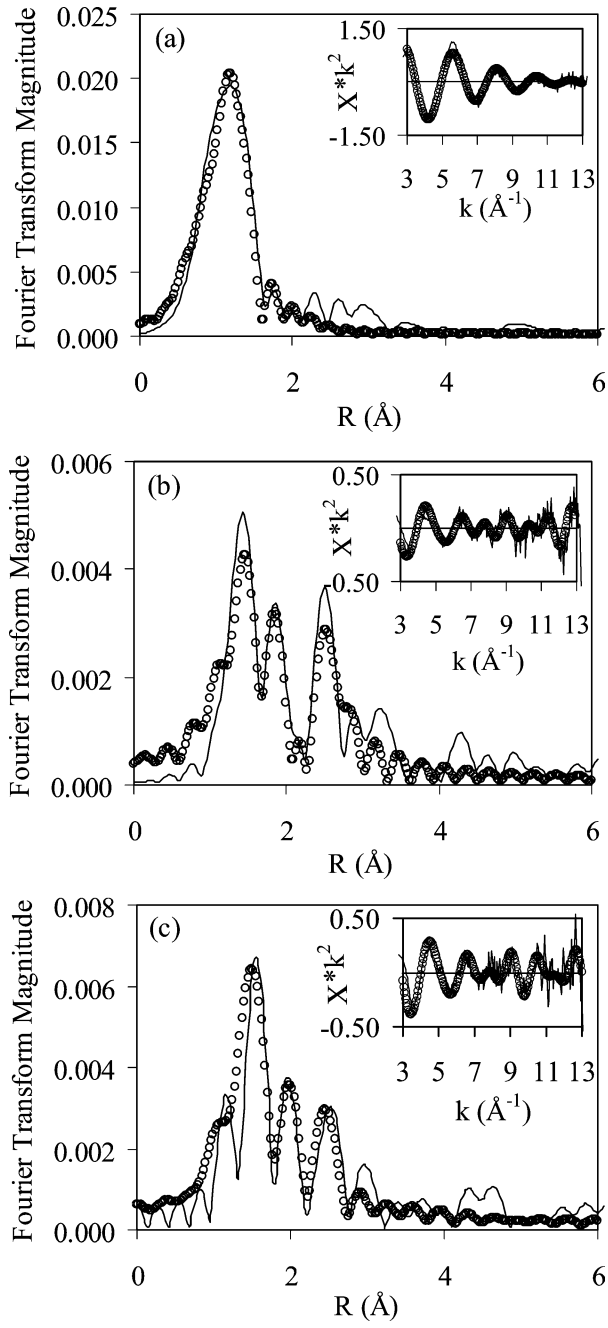

Fig. 10. Multiple scattering fit (circles) to Fourier-transformed k^2-weighted EXAFS for exchanged Mo/H-ZSM-5 ($Mo/Al_f = 0.41$, 950 K): (a) in 20% O_2/He, (b) carburized 1 h in CH_4, and (c) treated in a mixture with 0.025 CO_2/CH_4 for 1 h after (b). Insets show k^2-weighted EXAFS region. Solid lines in insets represent experimental data and circles represent fit.

Table 5
Refined structural parameters for Mo/H-ZSM-5 with different treatments

Mo/H-ZSM-5 treatment	Shell	Coordination number[a], this study	Interatomic distance (nm), this study	Coordination number[b], Ref. [19]	Interatomic distance (nm), Ref. [19]
20% O_2/He	Mo–O	1.0	0.17	1.0	0.169
	Mo–O	1.0	0.17	1.0	0.169
	Mo–O	1.0	0.18	1.0	0.178
	Mo–O	1.0	0.18	1.0	0.184
CH_4	Mo–C	1.7	0.20	–	–
	Mo–C	1.5	0.23	–	–
	Mo–C	0.2	0.24	–	–
	Mo–Mo	0.3	0.29	–	–
$CO_2/CH_4 = 0.025$	Mo–O	0.2	0.17	–	–
	Mo–C	1.9	0.21	–	–
	Mo–C	1.5	0.23	–	–
	Mo–Mo	0.2	0.28	–	–

[a] $S_0^2 = 0.77$, Debye–Waller factor fixed at zero, fit using k^2-weighted EXAFS.
[b] $S_0^2 = 0.63$, Debye–Waller factor fixed at zero, fit using k^1-weighted EXAFS.

gesting the presence of small clusters of a size similar to that found with those samples exposed to pure CH_4 reactants.

In Fig. 11, the time evolution of Mo structures obtained from principal component analyses of near-edge spectra is shown together with the amount of extraframework oxygen as measured by mass spectrometry as the composition of the reactant stream was varied with time. In the left panel, fresh $Mo_2O_5^{2+}$-ZSM-5 was exposed to a 50% CH_4/He stream (1 bar, 950 K; 5.8 $cm^3\,s^{-1}\,g_{cat}^{-1}$) within the X-ray absorption reactor cell and within a laboratory reactor in separate experiments. The data shown represent the fraction of the Mo atoms present as $Mo_2O_7^{2-}$ and MoC_x, calculated with the use of $MgMo_2O_7$ and bulk Mo_2C near-edge spectra as standards for the near-edge spectral analysis. Changes in the number of O atoms removed coincided with changes in the local coordination and the oxidation state of Mo atoms measured from near-edge spectra.

After catalysts were fully carburized, the reactant stream was changed to a CO_2/CH_4 mixture with a ratio of 0.025 (shown in the right panel). Here again, changes in the near-edge spectra occurred within the same time scale as the addition of O atoms measured by mass spectrometry (the initial lag in the change in MoO_x phase measured from X-ray absorption reflects differences in the time required for the new stream to reach the sample). After approximately 2.5 ks, the oxidation of MoC_x clusters stops and CO_2–CH_4 reforming near the bed inlet and CH_4 pyrolysis near the bed outlet reach steady-state rates. These data do not allow unequivocal structural identification because the predominant Mo phase changes with CO_2 concentration along the reactor. The oxidized Mo phase may form precursor-like $Mo_2O_5^{2+}$ species at sufficiently high CO_2 concentrations or MoO_2 clusters, as also occurs during deactivation of bulk Mo_2C at stoichiometric CO_2-reforming feeds [28]. The appearance of a pre-edge feature in the near-edge spectra for Mo-ZSM-5 samples exposed to 0.025 CO_2/CH_4 reactants (Fig. 8) suggests that Mo_2C oxidizes to volatile MoO_3 within regions of

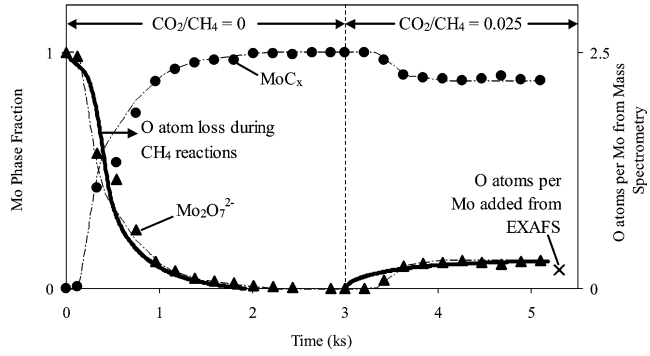

Fig. 11. Mo phase fraction as a function of time on $Mo_2O_5^{2+}$-ZSM-5 ($Mo/Al_f = 0.41$). The Mo phase fraction (denoted with symbols connected with broken lines) was determined using a least square's fit of $MgMo_2O_7$ and Mo_2C near-edge reference spectra to Mo-ZSM-5 catalysts in different oxidizing environments: 50 kPa CH_4 with 0 kPa (left) and 1.3 kPa (right) CO_2 at 950 K, 5.8 $cm^3\,s^{-1}\,g_{cat}^{-1}$. Solid lines indicate O/Mo ratios in the catalyst measured using on-line mass spectrometry (1 g, $Mo/Al_f = 0.41$, 950 K, 5.8 $cm^3\,s^{-1}\,g_{cat}^{-1}$, 54 kPa CH_4) with 0 kPa (left) and 1.2 kPa (right) CO_2.

the sample containing high enough CO_2 concentrations because MoO_2 has no pre-edge feature. These MoO_3 species would then redisperse to form the Mo-oxo dimers present in the starting material while the rest of the catalyst continues to function as fully carburized clusters active in CH_4 pyrolysis reactions.

4. Conclusions

The improvement in the stability of MoC_x-ZSM-5 catalysts resulting from the addition of an oxidant such as CO_2 at low concentrations to CH_4 feeds is a result of the H_2 formed by CO_2–CH_4 reactions. CH_4 reacts with CO_2 exclusively at the beginning of the bed; this reaction occurs via scavenging of surface C* and inhibits C–C bond formation. After CO_2 is completely consumed, pyrolysis products are formed at

lower yields as a result of H_2 formed in the CO_2–CH_4 section of the bed; H_2 decreased equilibrium yields to products and increased hydrogenation rates of surface species, preventing formation of carbonaceous deposits that have been linked to catalyst deactivation.

X-ray absorption and transient addition/removal of O atoms during CO_2 addition/removal to CH_4 streams provided strong evidence that Mo was oxidized to MoO_xC_y. Oxidized molybdenum carbide clusters formed remained active for CO_2 reforming below CO_2/CH_4 molar ratios of 0.1. The structure of the catalyst in CO_2/CH_4 feeds, determined from multiple scattering simulations of the radial scattering function, resembles that of 0.6 nm MoC_x clusters with a Mo–O coordinative shell at 0.17 nm. At CO_2 concentrations above 0.1 CO_2/CH_4, the catalyst became inactive, apparently the result of molybdenum oxide formation, but catalytic activity was restored in pure CH_4 after the removal of oxygen added during CO_2/CH_4 feeds.

Acknowledgments

The authors acknowledge the assistance of Dr. Félix Requejo with the collection and analysis of X-ray absorption data. Portions of this research were carried out at the Stanford Synchrotron Research Laboratory, a national user facility operated by Stanford University on behalf of the US Department of Energy, Office of Basic Energy Sciences. The authors acknowledge partial support by BP as part of the Berkeley-Caltech Methane Conversion Cooperative Program under the stewardship of Dr. Theo Fleisch. Howard Lacheen acknowledges with thanks the financial support of the Ford Corporation through the Ford Catalysis Fellowship administered by the Berkeley Catalysis Center.

References

[1] F. Kapteijn, G. Marban, J. Rodriguez-Mirasol, J.A. Moulijn, J. Catal. 167 (1997) 256.
[2] T. Mole, J.R. Anderson, G. Creer, Appl. Catal. 17 (1985) 141.
[3] S.N. Bulford, E.E. Davies, US Patent 4,157,356 (1979).
[4] R. Gregory, A.J. Kolombos, US Patent 4,056,575 (1977).
[5] M.S. Scurrell, Appl. Catal. 41 (1988) 89.
[6] Y. Ono, K. Kanae, J. Chem. Soc., Faraday Trans. 87 (1991) 663.
[7] R. Shigeishi, A. Garforth, I. Harris, J. Dwyer, J. Catal. 130 (1991) 423.
[8] M. Guisnet, N.S. Gnep, D. Aittaleb, J.Y. Doyemet, Appl. Catal. 87 (1992) 255.
[9] H. Kitagawa, Y. Sendoda, Y. Ono, J. Catal. 101 (1986) 12.
[10] G.L. Price, V.I. Kanazirev, J. Catal. 126 (1990) 267.
[11] Y. Ono, K. Kanae, J. Chem. Soc., Faraday Trans. 87 (1991) 669.
[12] K.M. Dooley, G.L. Price, V.I. Kanazirev, V.I. Hart, Catal. Today 31 (1996) 305.
[13] B.S. Kwak, W.M.H. Sachtler, J. Catal. 145 (1994) 456.
[14] Y. Ono, H. Kitagawa, Y. Sendoda, J. Chem. Soc., Faraday Trans. I 89 (1987) 2913.
[15] L. Wang, L. Tao, M. Xie, G. Xu, Catal. Lett. 21 (1993) 35.
[16] D. Wang, J.H. Lunsford, M.P. Rosynek, Top. Catal. 3 (1996) 289.
[17] R.W. Borry, Y.-H. Kim, A. Huffsmith, J.A. Reimer, E. Iglesia, J. Phys. Chem. B 103 (1999) 5787.
[18] Y.-H. Kim, R.W. Borry, E. Iglesia, Micropor. Mesopor. Mater. 35 (2000) 495.
[19] W. Li, G.D. Meitzner, R.W. Borry, E. Iglesia, J. Catal. 191 (2000) 373.
[20] F. Solymosi, A. Erdöhelyi, A. Szöke, Catal. Lett. 32 (1995) 43.
[21] B.M. Weckhuysen, D.J. Wang, M.P. Rosynek, J.H. Lunsford, J. Catal. 175 (1998) 338.
[22] Y. Shu, H. Ma, R. Ohnishi, M. Ichikawa, Chem. Commun. (2003) 86.
[23] W. Ding, G.D. Meitzner, E. Iglesia, J. Catal. 206 (2002) 14.
[24] R. Ohnishi, S. Liu, Q. Dong, L. Wang, M. Ichikawa, J. Catal. 182 (1999) 92.
[25] Y. Shu, R. Ohnishi, M. Ichikawa, J. Catal. 206 (2002) 134.
[26] Z. Liu, M.A. Nutt, E. Iglesia, Catal. Lett. 81 (2002) 271.
[27] B.M. Weckhuysen, M.P. Rosynek, J.H. Lunsford, Catal. Lett. 52 (1998) 31.
[28] J.B. Claridge, A.P.E. York, A.J. Brungs, C. Marquez-Alvarez, J. Sloan, S.C. Tsang, M.L.H. Green, J. Catal. 180 (1998) 85.
[29] H.S. Lacheen, E. Iglesia, Phys. Chem. Chem. Phys., in press.
[30] M. Boudart, G. Djega-Mariadassou, Kinetics of Heterogeneous Catalytic Reactions, Princeton University Press, Princeton, NJ, 1984.
[31] G.D. Meitzner, E. Iglesia, Catal. Today 53 (1999) 433.
[32] D.G. Barton, S.L. Soled, G.D. Meitzner, G.A. Fuentes, E. Iglesia, J. Catal. 181 (1999) 57.
[33] J.S. Lee, S.T. Oyama, M. Boudart, J. Catal. 106 (1987) 125.
[34] K. Stadnicka, Acta Cryst. B 33 (1977) 3859.
[35] WinXAS, v. 2.1 licensed by T. Ressler, Fritz Haber Institut der MPG, Dept. of Inorganic Chem., Faradayweg 4-6, D-14195, Berlin, Germany (email: t_ressler@winxas.de).
[36] M. Newville, B. Ravel, D. Haskel, J.J. Rehr, A. Stern, Y. Yacoby, Physica B 208 (1995) 154.
[37] J.J. Rehr, R.C. Albers, S.I. Zabinsky, Phys. Rev. Lett. 69 (1992) 3397.
[38] B. Ravel, J. Synch. Rad. 8 (2001) 314.
[39] E.R. Malinowski, Factor Analysis in Chemistry, Wiley, New York, 2002.
[40] T. Ressler, J. Wong, J. Roos, I. Smith, Environ. Sci. Tech. 34 (2000) 950.
[41] Chemkin Collection Software, v. 3.6 licensed by Reaction Design, 6440 Lusk Blvd., Suite D-209, San Diego, CA, 92121.
[42] D.R. Lide, CRC Handbook of Chemistry and Physics, 75 ed., CRC Press, Boca Raton, 1994.
[43] W.W. Akres, D.P. Camp, AIChE J. 1 (1955) 471.
[44] J. Wei, E. Iglesia, J. Catal. 224 (2004) 370.
[45] W. Ding, S. Li, G.D. Meitzner, E. Iglesia, J. Phys. Chem. B 105 (2001) 506.
[46] D. Ma, D. Wang, L. Su, Y. Shu, Y. Xu, X. Bao (2002).
[47] T. Ressler, O. Timpe, T. Neisius, J. Find, G. Mestl, M. Dieterle, R. Schlögl, J. Catal. 191 (2000) 75.
[48] T. Ressler, R.E. Jentoft, J. Wienold, M.M. Günter, O. Timpe, J. Phys. Chem. B 104 (2000) 6360.
[49] M.J. Fay, A. Proctor, D.P. Hoffmann, M. Houalla, D.M. Hercules, Mikrochim. Acta 109 (1992) 281.
[50] F.W. Kutzler, C.R. Natoli, D.K. Misemer, S. Doniach, K.O. Hodgson, J. Chem. Phys. 73 (1980) 3274.
[51] M. Fernández-García, C.M. Alvarez, G.L. Haller, J. Phys. Chem. 99 (1995) 12565.
[52] S.R. Wasserman, J. Phys. IV 7 (1997) 203.